

SPATIO-TEMPORAL MODELLING OF EXTREME STORMS¹

BY THEODOROS ECONOMOU,
 DAVID B. STEPHENSON AND CHRISTOPHER A. T. FERRO

University of Exeter

A flexible spatio-temporal model is implemented to analyse extreme extra-tropical cyclones objectively identified over the Atlantic and Europe in 6-hourly re-analyses from 1979–2009. Spatial variation in the extremal properties of the cyclones is captured using a 150 cell spatial regularisation, latitude as a covariate, and spatial random effects. The North Atlantic Oscillation (NAO) is also used as a covariate and is found to have a significant effect on intensifying extremal storm behaviour, especially over Northern Europe and the Iberian peninsula. Estimates of lower bounds on minimum sea-level pressure are typically 10–50 hPa below the minimum values observed for historical storms with largest differences occurring when the NAO index is positive.

1. Introduction. Extreme North Atlantic and European extra-tropical cyclones are a major source of risk for society. These natural hazards cause much damage and insurance loss in Europe due to extreme wind speeds/flooding. Recent examples include the December 1999 windstorms Anatol and Lothar [Ulbrich et al. (2001)], and windstorm Kyrill in 2007 which resulted in large losses across most of Europe. Important scientific questions are as follows:

1. How extreme (intense) can extra-tropical cyclones become? Or, more precisely, how much more extreme compared to the most extreme values recorded in short series of historical observations/analyses?
2. How does the extreme behaviour vary spatially?
3. How does the extreme behaviour vary in time due to modulation by large-scale climate patterns?

Received December 2012; revised June 2014.

¹Supported by the project RACEWIN, which was funded by the AXA research fund.

Key words and phrases. Bayesian hierarchical model, spatial random effects, natural hazards, extra-tropical cyclones, extreme value distribution, European windstorms.

This is an electronic reprint of the original article published by the Institute of Mathematical Statistics in *The Annals of Applied Statistics*, 2014, Vol. 8, No. 4, 2223–2246. This reprint differs from the original in pagination and typographic detail.

We consider sea-level pressure (i.e., cyclone depth) as a measure of cyclone intensity. Unfortunately, there are no simple physical arguments for how deep an extra-tropical cyclone can become. The most extreme events often deepen *explosively* with rapid decreases in central pressure, for example, storms known as *bombs* having pressure drops of more than 24 hPa in 24 hours at 60 N. Explosive cyclogenesis depends on many factors, for example, the deepest recorded 20th century low of 913 hPa (the Braer cyclone of January 1993) deepened 78 hPa in 24 hours due to a combination of several factors such as available moisture and stratospheric conditions [Odell et al. (2013)]. The unlikely possibility that such conditions could be maintained for 2 days gives a minimum value of SLP of around $990 - 156 = 834$ hPa starting from a typical background state of 990 hPa. It should also be noted that SLP less than 650 hPa would correspond to mid-latitude geostrophic wind speeds faster than the speed of sound, which due to shock wave dissipation would be impossible to maintain energetically. In the absence of any more rigorous physical bounds, it is of interest to estimate bounds empirically using statistical approaches such as extreme value theory.

Modelling cyclones poses an interesting challenge: the events occur irregularly in space and time with rates and magnitudes that are spatially heterogeneous and nonstationary in time (due to modulation by large-scale climate conditions). Furthermore, at any one location, very few extreme events are observed in short historical data sets. Here we model extreme North Atlantic cyclones using an extended version of the spatial point process model for extremes from Cooley and Sain (2010). The extension involves the inclusion of temporal covariates, the adaptation to irregularly occurring (i.e., random occurrence rather than fixed locations) extremes in space and the application to extra-tropical cyclones.

2. Background and data.

2.1. *Extreme extra-tropical cyclones.* There has been surprisingly little use of extreme value theory to investigate extreme cyclones [see Katz (2010) for a discussion about the lack of extreme value theory in climate science]. Lionello, Boldrin and Giorgi (2008) investigated changes in future cyclone climatology over Europe using the Generalised Extreme Value (GEV) distribution to model pressure minima. Return levels were calculated over the whole North Atlantic domain without explicit characterisation of spatial or temporal heterogeneity. Della-Marta and Pinto (2009) and Della-Marta et al. (2009) used a Generalised Pareto Distribution (GPD) model to analyse future changes in extreme wind intensity. Three large nonoverlapping areas were considered, however, there was no formal consideration of spatial or temporal variation in the extremes. Sienz et al. (2010) used GPD models

extending the work by Della-Marta and Pinto (2009) to include temporal covariates such as the North Atlantic Oscillation (NAO) and a linear trend but did not account for spatial variability. Bonazzi et al. (2012) used bivariate extreme value copulas to model the spatial dependence in footprints of peak gust wind speeds from a set of 135 damaging European cyclones. However, this study did not explicitly model the magnitude of many cyclones and so does not answer the question about upper bounds on cyclone magnitudes.

2.2. Brief review of spatial extreme models. Davison, Padoan and Ribatet (2012) identified three main classes of statistical models for spatial extremes: Bayesian hierarchical models (BHM), copula based models and max-stable process models. Although max-stable processes explicitly characterise spatial dependence, BHM can be more flexible and pragmatic by allowing for inclusion of physical mechanisms in terms of covariates and random effects. The major issue with BHM is the conditional independence assumption of the extremes, whereas for max-stable processes it is model implementation and flexibility. Copula models lie somewhere in between since the dependence of the extremes is modelled by the copula assuming that the marginal distributions are separable from this dependency structure [Sang and Gelfand (2010)].

In this paper, we adapt BHM as the modelling framework mainly because of their flexibility in allowing for (temporal) covariate effects along with a versatile spatial dependency structure through random effects. BHM generally assume independence of the extremes for given values of the covariates and random effects (conditional independence), although they can be extended to model spatial extremal dependence by including max-stable processes [Reich and Shaby (2012)]. For the application to extra-tropical cyclones, we believe conditional independence to be a reasonable working assumption. Much of the dependency between successive cyclones has been shown to be induced by modulation of rates by time-varying climate modes and so can be accounted for by including appropriate covariates [Mailier et al. (2006), Vitolo et al. (2009)].

There has been recent interest in spatial BHM for extremes since their introduction by Casson and Coles (1999). In Cooley, Nychka and Naveau (2007) and Cooley and Sain (2010), a GPD and a point process model are used to model extreme precipitation where the spatial dependence is characterised by Gaussian random effects in the formulation of model parameters but without incorporating temporal nonstationarity. Gaetan and Grigoletto (2007), Heaton et al. (2011) and Sang and Gelfand (2009) allowed temporal structure in BHM through time-varying covariates where the conditional model is a GEV distribution. Turkman, Turkman and Pereira (2010) used a similar model where the conditional model is a GPD. In this paper, we use the computationally efficient MCMC algorithm from Cooley and Sain (2010)

based on recent work on Markov random fields [Rue and Held (2005)] and add temporal covariates, to account for temporal trends and variations. We use the point process model for extremes as the conditional model: it utilises more of the data than GEV models and, unlike GPD models, inference is invariant to the choice of threshold.

2.3. Data. Objective feature-identification software [Hodges (1994)] was used to extract cyclone tracks from 6-hourly National Center for Environmental Prediction Climate Forecast System (NCEP-CFS) re-analysis data [Saha et al. (2010)] available over the period 1979–2009. Individual cyclone tracks are identified by tracking local maxima in relative vorticity just above the boundary layer (about 1.5 km above sea level). The minimum sea-level pressure (MSLP) and its location are recorded every 6 hours throughout the lifecycle of each cyclone. We use sea-level pressure as a measure of cyclone intensity mainly because this variable is well observed and has smooth variation during the lifetime of a cyclone, unlike other possible variables such as wind speed or vorticity. Figure 1(a) shows a map of cyclone tracks defined by 6-hourly MSLP recordings for a period with high cyclone activity. Only a subset of tracks is plotted: ones where any 6-hourly MSLP value reached below 960 hPa. Typical damaging cyclones over Europe reach values in the range 940–970 hPa, for instance, Anatol: 953 hPa [Ulbrich et al. (2001)] and Kyrill: 962 hPa [Mitchell-Wallace and Mitchell (2007)], whereas the lowest ever recorded Braer cyclone reached 913 hPa off the North–West of Scotland in January 1993 [Odell et al. (2013)].

Although wind speed could also have been used, exploratory analysis suggests that extreme MSLP and maximum wind speed are strongly dependent, as to be expected from simple balance arguments. Above the surface boundary layer outside equatorial regions, centrifugal and Coriolis forces are approximately balanced by the pressure gradient force. Hence, wind speeds above the boundary layer in extra-tropical cyclones are proportional to pressure gradients (gradient wind balance). Surface pressure gradients in turn are strongly related to the cyclone MSLP since extra-tropical cyclones have similar synoptic spatial dimensions (the so-called Rossby scale). Hence, from such simple dynamical meteorology arguments, MSLP and maximum wind speeds are expected to be extremally dependent and so will convey similar information. Let random variables W and Z denote maximum (6-hourly) wind speeds at about 1.5 km above the surface (on the 925 hPa pressure surface) and negated MSLP (obtained by multiplying MSLP by -1), respectively, with associated 6-hourly recorded values w_t and z_t . Figure 2(a) shows a plot of w_t against z_t : there is strong positive association with the loess smoother indicating a nearly linear relationship. To better visualise extremal dependence, Figure 2(b) shows the empirical copula obtained by producing

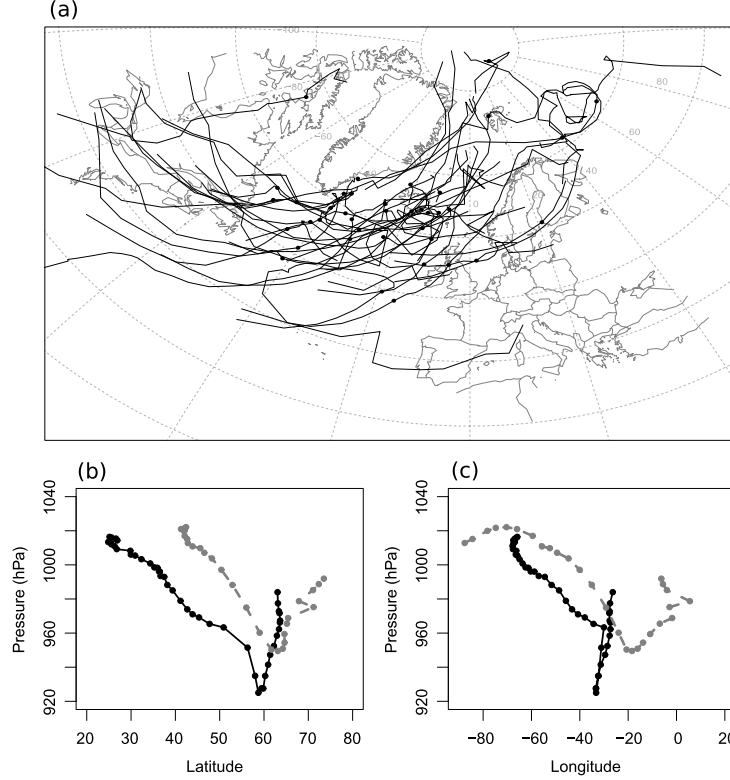


FIG. 1. (a) *Cyclone tracks for the October 1989 to March 1990 extended winter. Only a subset of tracks is plotted: ones where any 6-hourly MSLP value reached below 960 hPa. Nadir positions are denoted with solid circles.* (b) *Sea-level pressure versus latitude and* (c) *latitude for two of the cyclone tracks in (a).*

a scatter plot of the empirical probabilities $q_t^{(z)} = (\text{rank}(z_t) - 1)/(n - 1)$ and $q_t^{(w)}$ [Stephenson et al. (2008)], where n is the total number of 6-hourly recorded values. This transforms out the margins to uniform distributions since $q_t^{(z)}$ and $q_t^{(w)}$ are estimates of the cumulative distribution functions (CDFs) $F_Z(Z)$ and $F_W(W)$. Strong dependence of the extremes is evident from the convergence of the points in the upper right-hand corner of the graph.

Figure 2(c) shows estimates of the extremal dependence measure χ [Coles, Heffernan and Tawn (1999)] defined as $\chi = \lim_{p \rightarrow 1} \chi(p)$, where $\chi(p) = \Pr(F_Z(Z) > p | F_W(W) > p)$. As $p \rightarrow 1$, $\chi(p) \rightarrow 0$, implying asymptotic independence, so we also show $\bar{\chi}(p)$, another measure of strength of extremal dependence, in Figure 2(d). The quantity $\bar{\chi} = \lim_{p \rightarrow 1} \bar{\chi}(p)$ measures the strength of extremal dependence within the class of asymptotic independence. Since $\bar{\chi}(p)$ remains positive but does not tend to 1, we conclude that

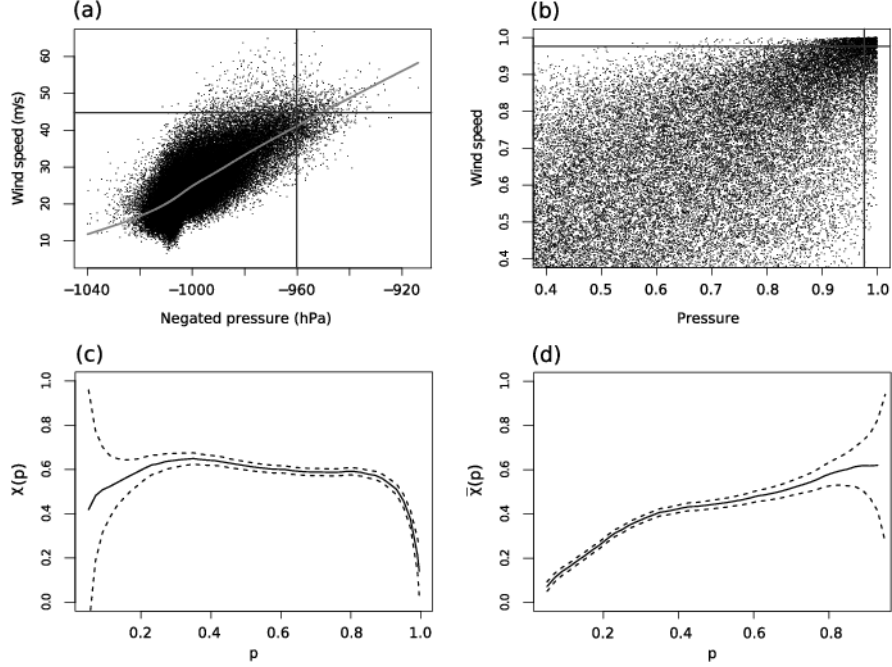


FIG. 2. (a) Wind speed against negated sea-level pressure with an associated loess fit (grey line). The intersecting lines are the values -960 hPa and 45 m/s for pressure and wind speed, respectively, representing the same high empirical quantile for each variable. (b) Empirical copula of wind speed and pressure along with the associated quantile lines from (a). (c) The associated extremal dependency measure $\chi(p)$, and (d) $\bar{\chi}(p)$ vs p . The 95% confidence intervals in (c) and (d) are based on the Normal approximation to proportions and are calculated as introduced in Coles, Heffernan and Tawn (1999).

there is a positive nonasymptotic association at extremes of negated MSLP and maximum wind speed, so either variable could potentially be used to investigate extremes (see Appendix A.2 for details on χ and $\bar{\chi}$).

Figure 1(b) and (c) show plots of MSLP against latitude and longitude, respectively, for two particular cyclone tracks in the 1989–1990 winter [Figure 1(a)]. The plots illustrate not only the tendency of intense cyclones to move in a west-to-north direction but also the fact that MSLP decreases (cyclone deepening) as the cyclone propagates in space and time, to reach a minimum (which we assume approximates the unobserved value of the cyclone nadir) before it starts increasing again until the end of the life cycle. Understanding the limiting strength of the nadirs is an important aspect in the study of extra-tropical cyclones. However, the rate of growth of cyclones depends on the large-scale atmospheric environment that they pass from, so the pressure limit of cyclone nadirs will vary with the spatial location of the cyclone. By only considering the nadir from each track, we focus on a

fundamental limiting property of cyclones, namely how deep they can get in general rather than how deep they can get in specific spatial locations. In other words, we are interested in spatial variation in cyclone intensity rather than maximum local cyclone impact.

The analysis of nadirs only, also helps to eliminate dependency between successive 6-hourly MSLP measures and reduces the amount of data from 313,557 6-hourly measurements to 17,230 nadirs. Figure 3(a) shows the (re-analysis) nadir from each track in the Atlantic region where dots in black are nadirs with sea-level pressure lower than 960 hPa. However, a single value for the threshold defining the extremes is not appropriate and the definition of extremeness should vary spatially. For example, a damaging cyclone in the Mediterranean is likely to be considered a weak one over Scandinavia.

Note that we use cyclone tracks from a reanalysis data set mainly because generally cyclone track observations for the extra-tropics are not readily available. However, reanalysis data are output from climate models with assimilated historical observational data. There is much smoothing/interpolation of the observational data when creating a reanalysis data set, so the interpretation of any results obtained here is conditional on the effects of such smoothing.

3. Model specification and model fitting.

3.1. *Spatial discretisation.* Conventional Bayesian spatial models generally rely on the assumption that data are either gridded or they come from fixed locations in space [see Banerjee, Carlin and Gelfand (2004)], where one or more observations are available at each location. Extreme nadirs, however, behave like a spatial marked point process where both location of occurrence and magnitude are random. To utilise such Bayesian models, we propose for simplicity to discretise space by imposing a finite grid and to consider the minimum possible size Δ for each grid cell, to ensure that enough data are available for estimation in each cell. Inference should not be sensitive to the choice of grid spacing, provided it is fine enough (in the limit $\Delta \rightarrow 0$ one should obtain the original marked point process). Sensitivity analysis for Δ is an important part of the concept (see Section 3.6).

For spatial marked point processes, estimation is only possible after making assumptions about spatial (and temporal) structure. The assumption made by discretising is that, conditional on a cell-specific random effect and possible covariates, the extreme events (nadirs) within each cell come from the same distribution. The cell-specific random effects are spatially dependent to allow for correlation between events in neighbouring cells. We also assume that the events can occur anywhere within the cells, with equal probability. Importantly, redefining space into discrete grid cells also provides a

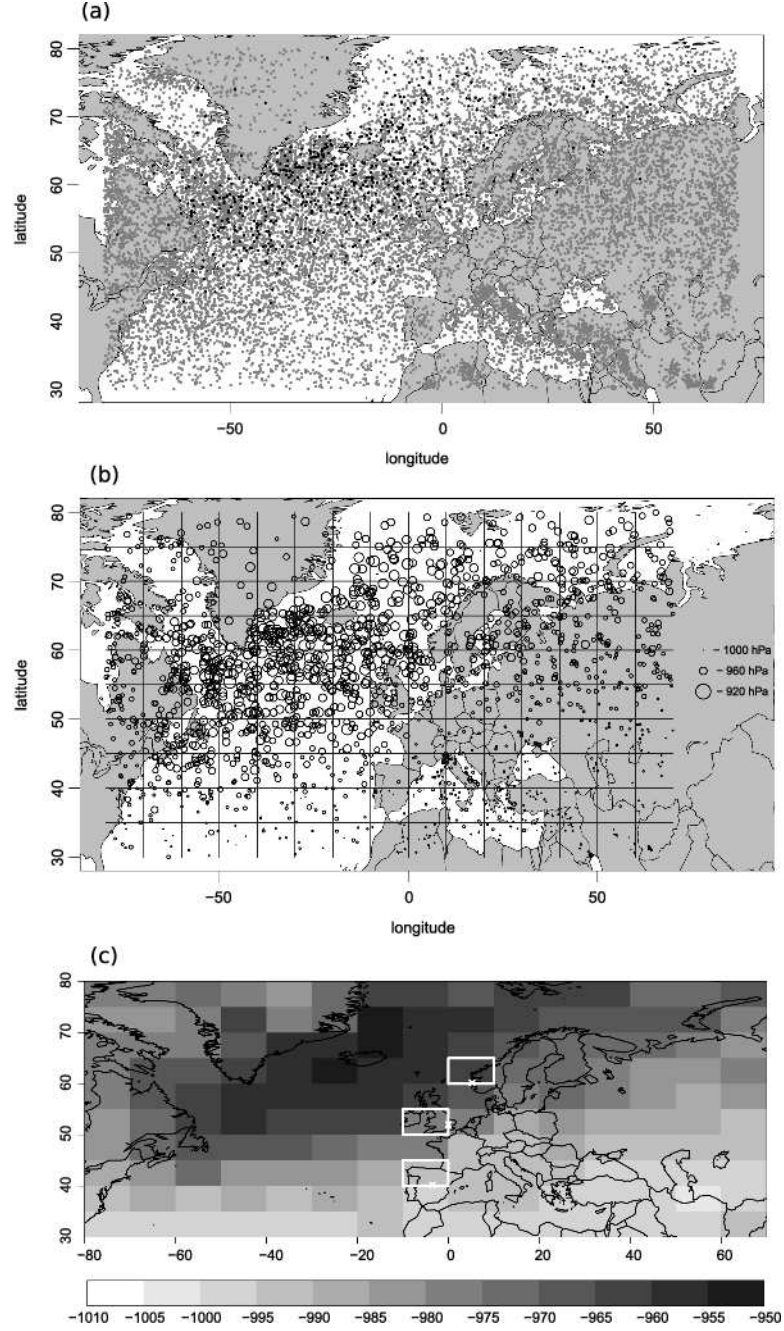


FIG. 3. (a) Map of all cyclone nadirs: dots in black represent nadirs deeper than 960 hPa, (b) map of recorded $X(s,t)$ that are greater than the threshold (90th empirical quantile) in each grid cell and (c) map of thresholds in each cell.

way of defining extremes in space: as values below a cell-varying threshold or as the $r = 1, 2, \dots$ largest values, in fixed time periods.

More generally, conditional on a given spatial or spatio-temporal dependence structure between cells, nadirs are modelled using an appropriate extreme value model. This is a hierarchical model where at the top of the hierarchy, random effects and covariates define a spatio-temporal process which modulates the process, giving rise to extreme nadirs.

3.2. Spatial grid. Conventionally, extreme value modelling is applied to the upper tails so the nadirs are negated to obtain variable $X(s, t)$, where s refers to the grid cell and t refers to time. We may think of $X(s, t)$ as the depth of a cyclone so that high values of $X(s, t)$ correspond to low values of MSLP. We divided the domain in Figure 3(a) into $N = 150$ $5^\circ \times 10^\circ$ grid cells. The threshold $u(s)$ in each cell was defined as the empirical 90th quantile of $X(s, t)$. We performed exploratory threshold analysis using mean residual life plots [Coles (2001)], ensuring that the 90th empirical quantile was an appropriate threshold choice. Figure 3(b) shows the map of the extremes (1736 nadirs) and Figure 3(c) shows the map of $u(s)$. Note that in Figure 3(c), three cells are highlighted: cells containing coordinates $(5.2^\circ\text{E}, 60.2^\circ\text{N})$, $(0^\circ\text{E}, 5^\circ\text{N})$ and $(3.5^\circ\text{W}, 40.2^\circ\text{N})$ marked in white crosses. These coordinates relate to the cities of Bergen, London and Madrid, respectively, and will be used throughout the paper for illustration of results, as they adequately span Europe in terms of latitude.

3.3. Model specification. To model the depth X of negated nadirs, we consider the point process model for extremes [Coles (2001)]—conditional on spatial random effects and temporal covariates. For some high threshold u of X , this model is parametrised in terms of the location, scale and shape parameters of the GEV distribution, namely, μ , σ and ξ (see Appendix A.1). We use the notation $X \sim \text{PP}(\mu, \sigma, \xi, u)$. Introducing spatial and temporal variation, let $X(s, t)$ be the depth in grid cell $s \in \mathbb{S}$ at time $t \in \mathbb{T}$, where \mathbb{S} and \mathbb{T} are the space and time domains, each a fixed subset of 2-dimensional and 1-dimensional Euclidean space, respectively. Extending the approach of Cooley and Sain (2010), we model the $X(s, t)$ in the following way:

$$\begin{aligned}
 (1) \quad & X(s, t) | \theta^\psi(s), \beta_2(s) \sim \text{PP}(\mu(s, t), \sigma(s, t), \xi(s), u(s)), \\
 (2) \quad & \mu(s, t) = \beta_0^\mu + \beta_1^\mu z_1(t) + \beta_2(s) z_2(t) + \theta^\mu(s), \\
 (3) \quad & \log(\sigma(s, t)) = \beta_0^\sigma + \beta_1^\sigma z_1(t) + \theta^\sigma(s), \\
 (4) \quad & \xi(s) = \beta_0^\xi + \theta^\xi(s)
 \end{aligned}$$

for $\psi = \mu, \sigma, \xi$. Defining vectors $\mathbf{U}^\psi = (U^\psi(1), \dots, U^\psi(N))'$ for $\psi = \mu, \sigma, \xi$, $\mathbf{U}(s) = (U^\mu(s), U^\sigma(s), U^\xi(s))'$ and $\mathbf{U} = (\mathbf{U}^\mu, \mathbf{U}^\sigma, \mathbf{U}^\xi)'$, the spatial level of

the model is as follows:

$$(5) \quad (\theta^\mu(s), \theta^\sigma(s), \theta^\xi(s))' | \mathbf{U}(s) \sim N(\mathbf{U}(s), \text{diag}(\boldsymbol{\tau})^{-1}),$$

$$(6) \quad \mathbf{U} = (\mathbf{U}^\mu, \mathbf{U}^\sigma, \mathbf{U}^\xi)' \sim N(\mathbf{0}, \boldsymbol{\Omega}^{-1}),$$

$$(7) \quad \beta_2(s) \sim N(\nu, \phi^2),$$

where z_1 is the latitude of the occurrence and z_2 is the North Atlantic Oscillation (NAO) value (see Section 3.4 about covariate selection). The spatial random effects $\theta^\mu(s)$, $\theta^\sigma(s)$ and $\theta^\xi(s)$ define spatial variability in μ , $\log(\sigma)$ and ξ across the cells, after allowing for covariates. The r -year return level, that is, the $(1 - 1/r)$ th quantile of $X(s, t)$ in cell s and time t , is given by

$$(8) \quad X_{1-1/r}(s, t) = \mu(s, t) + \frac{\sigma(s, t)}{\xi(s)} ((-\log(1 - 1/r))^{-\xi(s)} - 1).$$

As in Cooley and Sain (2010), vectors \mathbf{U}^ψ are modelled jointly using a separable formulation [Banerjee, Carlin and Gelfand (2004), Chapter 7], so that the precision matrix is $\boldsymbol{\Omega} = \mathbf{T} \otimes \mathbf{W}$. The matrix \mathbf{T} is an unknown 3×3 positive definite symmetric matrix and \mathbf{W} is an $N \times N$ proximity matrix defining spatial proximity between the N cells. Therefore, the dimension of $\boldsymbol{\Omega}$ is $3N \times 3N$. Here, spatial proximity is based on nearest neighbours so that off-diagonal elements of \mathbf{W} are $w_{i,j} = -1$ if cells i and j are adjacent and $w_{i,j} = 0$ otherwise, whereas diagonal elements $w_{i,i} = -\sum_{i \neq j} w_{i,j}$ [see Bailey and Gatrell (1995), pages 261–262 for other examples of proximity measures].

Each vector $\mathbf{U}^\mu, \mathbf{U}^\sigma, \mathbf{U}^\xi$ is modelled by an Intrinsic AutoRegressive (IAR) spatial model [Banerjee, Carlin and Gelfand (2004)]. The IAR model uses the proximity matrix and a single unknown parameter to control the spatial dependency structure (see Appendix A.3). Here, there are three such parameters for each of $\mathbf{U}^\mu, \mathbf{U}^\sigma, \mathbf{U}^\xi$ and they are found in the diagonal of \mathbf{T} . (Note that the value of $\boldsymbol{\tau}$ is conventionally fixed beforehand to avoid nonidentifiability between $\boldsymbol{\tau}$ and the diagonal of \mathbf{T} [Banerjee, Carlin and Gelfand (2004)].) Dependence between $\mathbf{U}^\mu, \mathbf{U}^\sigma, \mathbf{U}^\xi$ is modelled using 3 parameters, the off-diagonals of \mathbf{T} , each controlling the strength of dependence. Allowing explicitly for this dependence can aid the MCMC estimation discussed in Section 3.5, in terms of convergence to the posterior and also mixing of the MCMC samples.

The NAO parameter $\beta_2(s)$ is spatially variable but in an unstructured way. This ensures that $\beta_2(s)$ share information to aid estimation in cells with few events but less so compared to using a structured (IAR) spatial prior. Parameter ν_k^ψ reflects the overall NAO effect on $\mu(s, t)$.

We complete the model specification by defining the prior distributions of the hyperparameters. The intercepts $\beta_0^\mu, \beta_0^\sigma, \beta_0^\xi$ were given Gaussian priors

with large variance, and means $(\bar{\mu}, \log \bar{\sigma}, \bar{\xi})$, calculated as means of independent maximum likelihood fits of point process models in each cell. For parameters $\beta_1^\mu, \beta_1^\sigma, \nu$, we assumed a flat Gaussian prior with zero mean and large variance. The prior distribution $\pi(\cdot)$ for ϕ_k^ψ is chosen so that $\pi(\phi_k^\psi) \propto 1/\phi_k^\psi$ [Gelman et al. (2013), Chapter 3], whereas for \mathbf{T} and \mathbf{P} we use a Wishart prior with 3 degrees of freedom (uninformative) and a mean that relates to the variability of μ , σ and ξ across cells (see Section 3.5).

3.4. Covariate selection. This was performed by adding explanatory variables to a “null” model: the model in (1)–(4) without z_1 or z_2 . Models were compared using the Deviance Information Criterion (DIC), a model selection criterion for Bayesian models [Spiegelhalter et al. (2002)] and by investigating whether posterior distributions of associated parameters are centred at zero with relatively large variance.

The model in (1)–(4) was first implemented with the addition of latitude, longitude, latitude squared, longitude squared and an interaction term between longitude and latitude as covariates in both $\mu(s, t)$ and $\log(\sigma(s, t))$. This allows for large-scale spatial trends, leaving the local spatial dependence to the random effects. It also relaxes the assumption of complete spatial randomness of extreme events within a cell, both in terms of occurrence and intensity. In principle, nonparametric surfaces can also be considered for smoothing large-scale spatial trends [see Davison, Padoan and Ribatet (2012), page 173 for references], but this was not deemed necessary here. To quantify the effect of large-scale climate patterns, two climate indices were also considered as covariates: the North Atlantic Oscillation (NAO) and the East Atlantic Pattern (EAP), both of which have been shown to be influential for extra-tropical cyclones [Mailier et al. (2006), Seierstad, Stephenson and Kvamsto (2006), Pinto et al. (2009), Nissen et al. (2010)]. No covariates were considered for the shape parameter $\xi(s)$ since this is a particularly difficult parameter to estimate, however, it was allowed to vary between cells. Out of all possible covariate combinations, the lowest DIC value occurred for the particular model formulation in (1)–(4). The posterior distributions of “insignificant” parameters (e.g., ones relating to longitude) had means and medians very close to zero.

It is well known that the NAO has influence on the development of extra-tropical cyclones [Pinto et al. (2009)]. By definition, the NAO index is standardised to have zero mean and unit variance, and here it was defined as 5-day nonoverlapping averages from 1979–2009. Figure 4(a) shows the time series of NAO and Figure 4(b) shows the histogram of NAO where the values of 2 and -2 are marked, as we consider these as high and low NAO threshold values throughout the rest of this paper. Figure 4(c) and (d) show extreme values of $X(s, t)$ for which $\text{NAO} \geq 2$ and $\text{NAO} \leq -2$, respectively. There is a clear North–South pattern in the Central Atlantic, implying NAO has a notable effect on extreme cyclones.

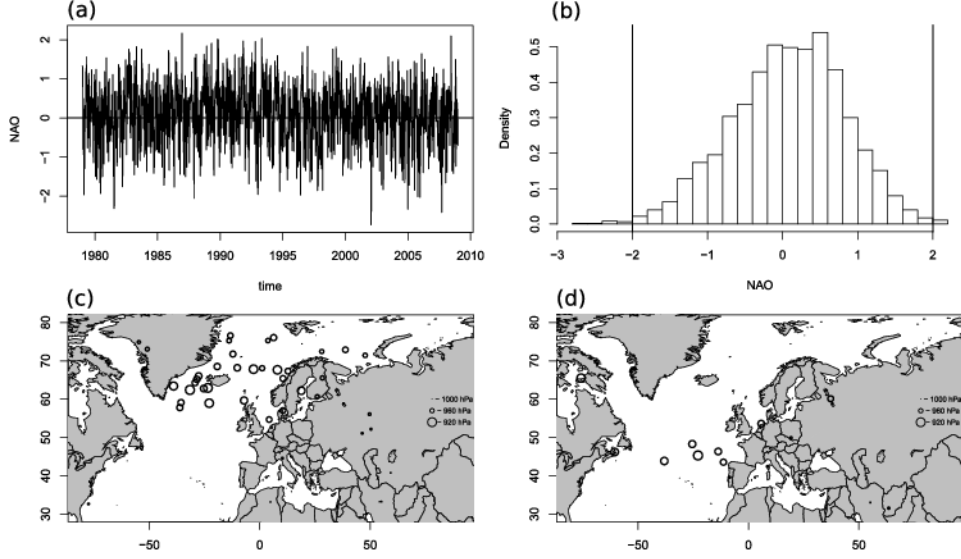


FIG. 4. (a) Time series of NAO defined as a 5-day average of daily NAO, (b) histogram of NAO along with vertical lines marking the values -2 and 2 , (c) occurrences of recorded nadirs where the associated NAO value was greater than 2 and (d) less than -2 .

3.5. Estimation by Markov chain Monte Carlo. For all $\psi = \mu, \sigma, \xi$, random effects $\theta^\psi(s)$ and $\beta_2(s)$, and parameters β_1^μ and β_1^σ , were sampled by Metropolis–Hastings, specifically using a random walk sampler. The intercepts β_0^ψ were sampled from their full conditionals using Gibbs sampling, by treating them as intercepts in the mean for each $\theta^\psi(s)$. Samples of $(\mathbf{U}^\mu, \mathbf{U}^\sigma, \mathbf{U}^\xi)'$ and \mathbf{T} were drawn using Gibbs sampling, utilising the specific techniques in Cooley and Sain (2010). Both ν and ϕ^2 were sampled from their full conditionals: Gaussian and scaled inverse- χ^2 , respectively.

Note that when the IAR model is used as a prior it is improper: the density does not integrate to 1. So, to make the intercept terms β_0^ψ identifiable, the rows of \mathbf{W} must sum to zero. This in turn imposes the restriction that $\sum_s U^\psi(s) = 0$.

The parameter $\boldsymbol{\tau}$ was set to $(0.1, 10, 100)'$. These values were chosen by fitting independent point process models in each cell and investigating the level of variability between cells for $\mu(s)$, $\log(\sigma(s))$ and $\xi(s)$, not only to reflect the difference in scale for the three parameters but also to make sure that most of the variability is modelled by the random effects $\mathbf{U}^\mu, \mathbf{U}^\sigma, \mathbf{U}^\xi$ and not $\boldsymbol{\tau}$. If values in $\boldsymbol{\tau}$ are too small, then the variability in each $\theta^\psi(s)$ is forcibly large and may cause problems in estimating the diagonal of \mathbf{T} which relates to the variability of each \mathbf{U}^ψ . Sensitivity analysis was performed to ensure these values have little effect on inference (not shown for conciseness).

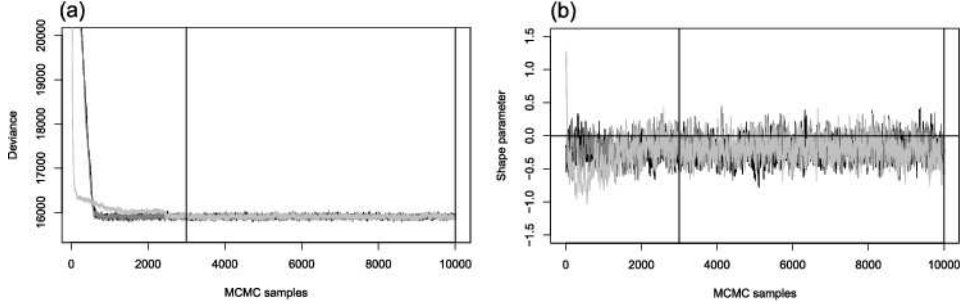


FIG. 5. (a) *Deviance samples from each of the three MCMC chains. Vertical lines denote the burn-in and the total number of simulations. Samples between the two lines are used for inference.* (b) *Samples of the shape parameter $\xi(s)$ for the grid cell containing London.*

The Wishart prior for the precision matrix \mathbf{T} was given the following mean: $\text{diag}(0.02, 4, 40)'$. As with τ , these values were calibrated by fitting independent point process models and were chosen to reflect the associated levels of variability for each of $\mu(s)$, $\log(\sigma(s))$ and $\xi(s)$.

The model in (1)–(4) was implemented in R [R Development Core Team (2012)] using three parallel MCMC chains. These were run on a workstation with a 3.07 GHz i7 processor and the processing speed for each chain was 30 seconds for 1000 samples. A total of 50,000 samples were collected per chain and thinned by 5 to reduce auto-correlation. After thinning, the first 3000 samples from each chain were discarded based on a trace plot of deviance (minus twice the log-likelihood) shown in Figure 5(a). Convergence in the deviance is a good indication of convergence to the joint posterior of all parameters [Gelman et al. (2013)]. Summarising, 21,000 posterior samples were used to calculate posterior distribution statistics for the parameters. Figure 5(b) shows an example trace plot of $\xi(s)$ for the grid cell containing the London coordinate.

3.6. Sensitivity to grid cell size. A purely spatial model [i.e., model (1)–(4) without z_1 and z_2] and a stationary model [i.e., model (1)–(4) without z_1 , z_2 and the random effects] were implemented for different grid configurations. For each model, the 100-year return level (i.e., the level exceeded by the annual maximum in any particular year with probability 0.01) of $X(s, t)$ was calculated using (8), for each of the three coordinates marked in Figure 3(c). Figure 6 shows the posterior mean of the 100-year return level against the number of cells in each grid configuration along with 95% credible intervals for each model. Convergence of the return value, as the number of cells increases, is evident for the spatial model (although this varies slightly due to sampling variation). The random effects pool information spatially, whereas the stationary model ignores neighbouring cells, resulting

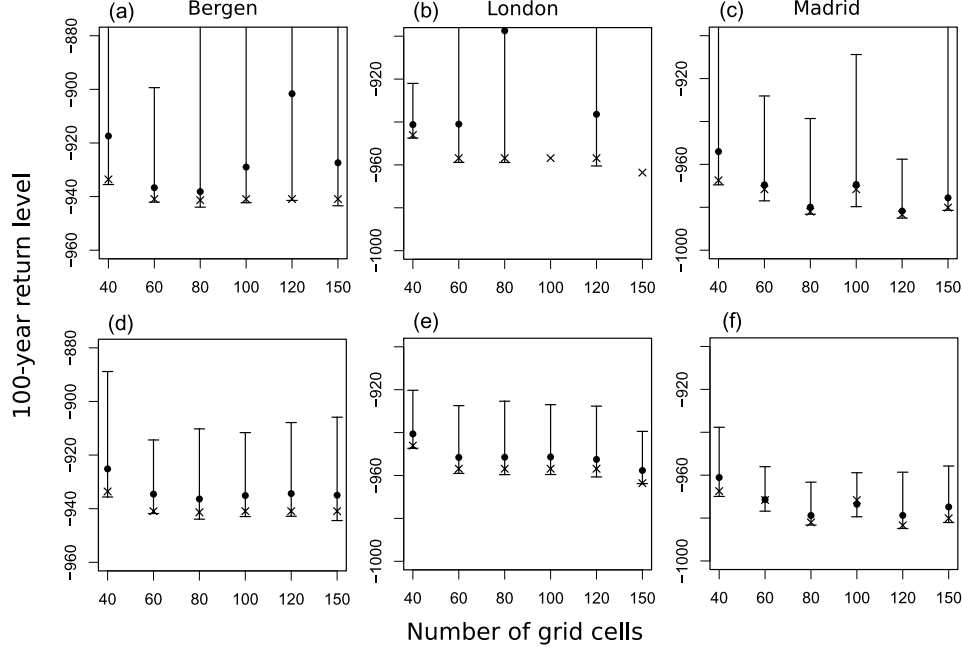


FIG. 6. Dots are posterior means of the 100-year return level of $X(s, t)$ versus number of cells in different grid specifications, along with 95% credible intervals. Left [(a) and (d)], middle [(b) and (e)] and right [(c) and (f)] panels refer to the Bergen, London and Madrid cells, respectively. Top [(a), (b), (c)] and bottom [(d), (e), (f)] panels refer to the stationary and the spatial models, respectively. For reference, the deepest recorded value of $X(s, t)$ in each cell is shown with a cross symbol.

in failure to converge, especially over London. Pooling also results in notably smaller credible intervals for the spatial model—note that the intervals are skewed. We chose $N = 150$ cells for the analysis so that all cells have an adequate number of nadirs (ranging from 14 to 376).

4. Results. Posterior distributions for global parameters are summarised in Table 1. Latitude has a positive linear effect on both the location and log-scale parameters of extreme cyclone depth $X(s, t)$. The overall NAO effect ν is positive, in agreement with findings from previous studies [Pinto et al. (2009)]. To assess MCMC convergence, the Gelman and Rubin \hat{R} multi-chain diagnostic was used for each of our model parameters [Gelman et al. (2013)]. The \hat{R} values for each parameter in Table 1 are all close to unity, suggesting convergence.

Figure 7 shows posterior means and standard deviations of $\mu(s, t)$, $\sigma(s, t)$ and $\xi(s)$. Much of the spatial structure in the extreme nadirs comes from the location and scale parameters. The posterior means for the shape parameter $\xi(s)$ are more uniform and generally negative, apart from one cell over

TABLE 1
Summary of parameter posterior distributions

Parameter	Prior	Posterior mean (s.e.)	95% Cr.I.	\hat{R}
β_1^μ (Latitude)	N(0, 100)	4.71 (0.62)	[3.61, 5.94]	1.13
β_1^σ (Latitude)	N(0, 100)	0.12 (0.07)	[0.00, 0.25]	1.03
Overall NAO effect ν	N(0, 100)	1.21 (0.24)	[0.77, 1.66]	1.01
Variance NAO effect ϕ^2	$\propto 1/\phi^2$	5.6 (1.85)	[3.09, 10.25]	1.00
β_0^μ	N(−944.1, 100)	−987.4 (0.51)	[−988.5, −986.5]	1.04
β_0^σ	N(5.7, 100)	2.03 (0.06)	[1.91, 2.15]	1.05
β_0^ξ	N(−0.19, 100)	−0.13 (0.03)	[−0.18, −0.07]	1.10

Iceland. Exploring this further, the two deepest nadirs in the reanalysis occurred in this cell, and they are considerably lower than the rest of the nadirs in the vicinity. A return level plot from the particular cell indicated that the two nadirs (one of them being from the record-breaking Braer cyclone) unduly influenced the sign of the shape parameter. This has been quantified by removing those two points and refitting the model, however, this being an analysis of extremes, it makes little sense to remove such values.

A negative shape parameter implies that the distribution of extreme cyclone depth $X(s, t)$, at time t and cell s , has an upper bound given by $\sigma(s, t)/\xi(s) - \mu(s, t)$. Here this corresponds to a lower limit on nadir sea-level pressure. Many of the posteriors for $\xi(s)$ do have some mass over the positive real line [see, e.g., Figure 5(b)]. However, except for the Iceland cell, the negative masses for $\xi(s)$ are all greater than 0.5, therefore, we can use the negative posterior $\xi(s)$ samples to obtain a conditional posterior distribution for the estimated lower limit. The posterior means of these limits are shown in Figure 8(c) for NAO = 0. The limit for the cell containing Bergen is 890.0 hPa [193.0, 932.6] and for the London cell it is 943.0 hPa [714.8, 959.4], whereas in the Madrid cell it is 953.5 hPa [537.9, 978.7]. The 95% credible intervals are skewed and noticeably wide, which is to be expected given we are trying to estimate the 100th percentile. The lower bounds on some of these intervals are too low to be physically plausible and this reflects the fact that the statistical model is not constrained by physical mechanisms. Note also that there is considerable literature focusing on the problem of estimating upper/lower bounds of distributions. See [de Haan and Ferreira \[\(2006\), Chapter 4\]](#) for a detailed discussion and a description of both maximum likelihood and moment estimators for bounds arising from extreme value distributions. In addition, Einmahl and Magnus (2008) provide refined estimators for bounds of world records in athletics and their respective sampling distributions.

The posterior means and standard deviations of the NAO effects $\beta_2(s)$ are shown in Figure 7(g) and (h), respectively. A positive effect is prominent in

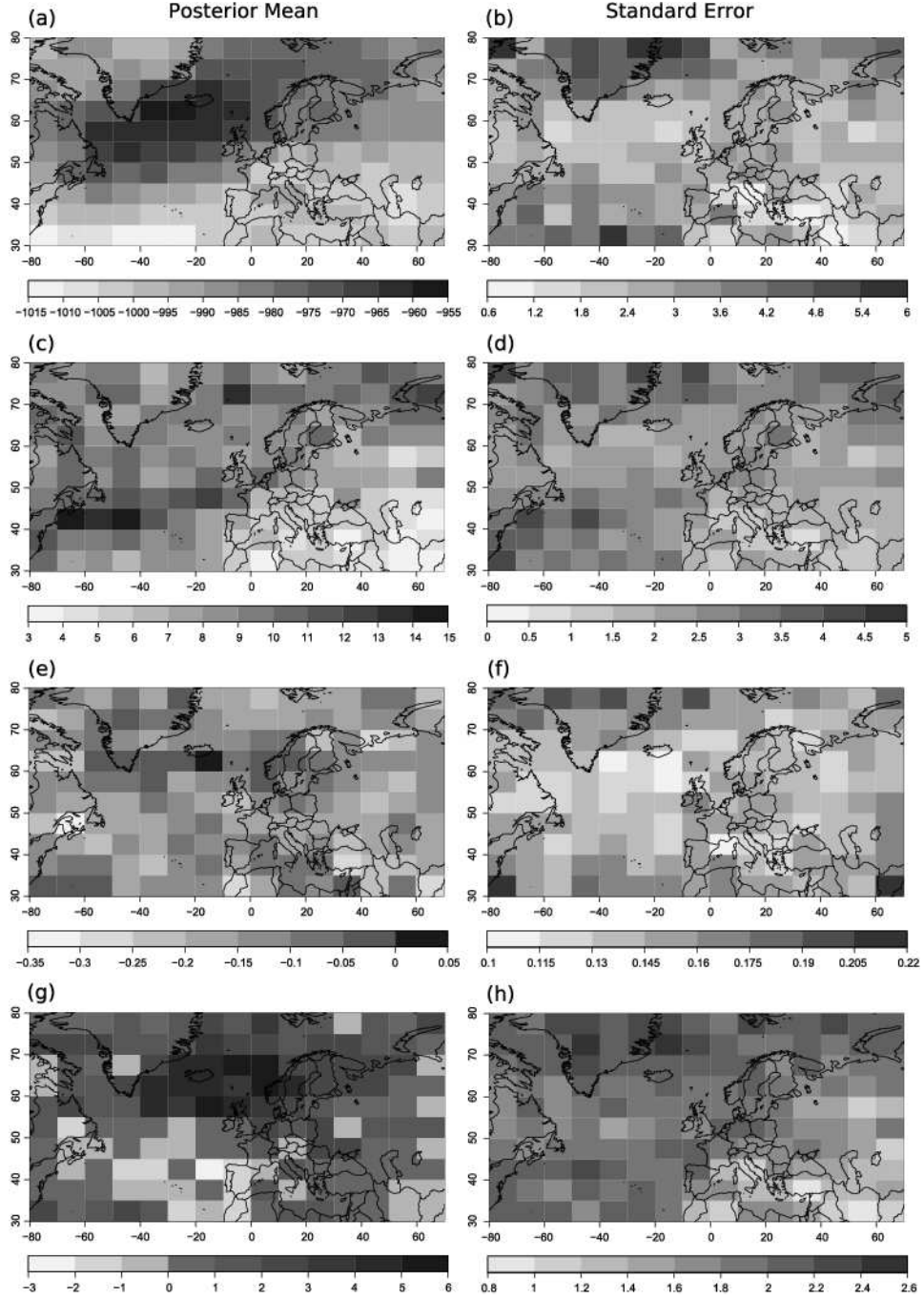


FIG. 7. Posterior means for (a) $\mu(s,t)$, (c) $\sigma(s,t)$, (e) $\xi(s)$ and (g) $\beta_2(s)$ and standard errors in (b), (d), (f) and (h), respectively, where $z_1(t)$ is latitude at centre of grid cell and $z_2(t) = 0$.

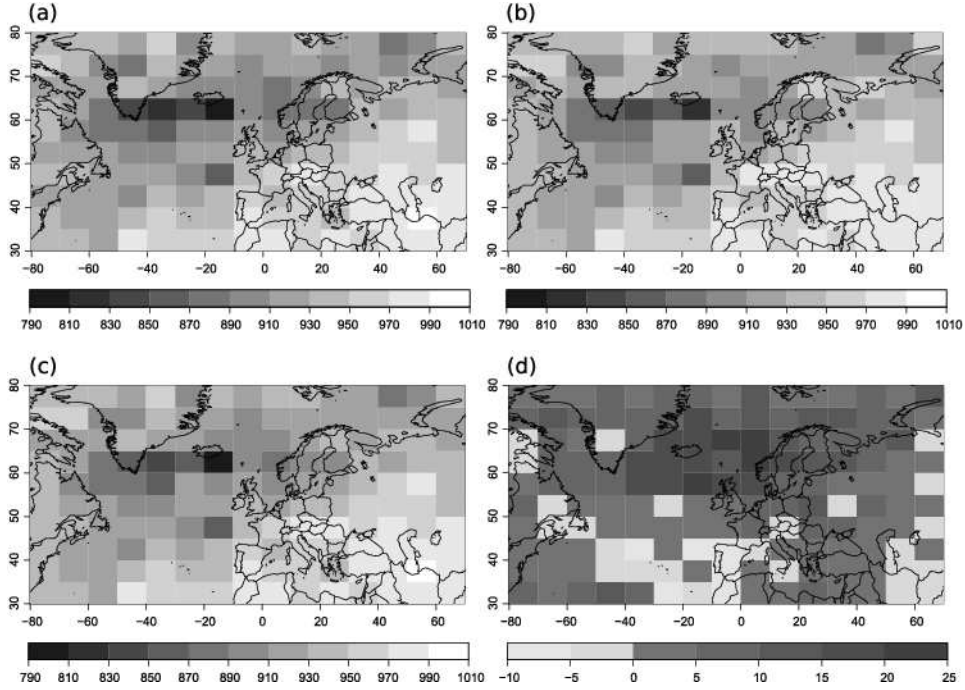


FIG. 8. *Estimated lower limits of nadir sea-level pressure for (a) NAO = 2, (b) NAO = -2 and (c) NAO = 0. (d) shows the difference between (a) and (b).*

the area where cyclones deepen the most: in the vicinity of Iceland, northern Europe and Scandinavia. A negative effect is also apparent, effectively over Spain and the Azores. This North–South NAO effect in the central Atlantic is consistent with the exploratory diagnostics in Figure 4(c) and (d). Maps of the estimated lower limit for NAO = -2 and NAO = 2 are given in Figure 8(a) and (b). To better see the effect of NAO on the estimated lower limit, Figure 8(d) shows the difference in hPa between the estimated lower limits for NAO = 2 and NAO = -2. The difference can get up to 25 hPa in the area where NAO has the biggest effect, that is, northern Europe and Scandinavia.

Figure 9 shows return level plots of $X(s, t)$ for the Bergen–London–Madrid grid cells, for NAO = ± 2 . Note that this is not a goodness-of-fit test, as each point in these plots (the recorded value) is associated with a different NAO value, whereas the return level curves are calculated at NAO = ± 2 . A positive/negative NAO effect is noticeable in the Bergen/Madrid cells, confirming the NAO North–South effect. No NAO effect is evident in the London cell. The horizontal line in each plot is the estimated cyclone depth limit, suggesting that for all three cells, nadirs could have been much deeper than the ones recorded.

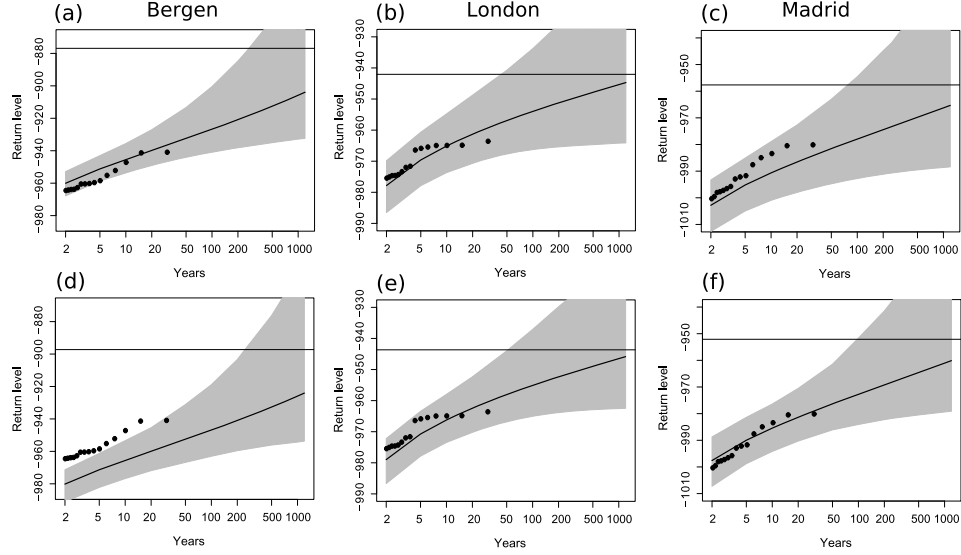


FIG. 9. Individual grid cell return level plots (posterior means) with 95% credible intervals. Observed values shown in solid circles. Top panel: NAO = 2; bottom panel: NAO = -2. Left panel: Bergen cell; middle panel: London cell; right panel: Madrid cell. Horizontal lines are estimated upper bounds of $X(s, t)$ for NAO = 2 (top) and NAO = -2 (bottom).

Therefore, we also consider the quantity $\pi(s, t) = \Pr(X(s, t) > x_m(s))$, where $x_m(s)$ is the negated minimum recorded nadir in grid cell s for the 30-year period. (Note that this is equivalent to describing how unusual the recorded depth was, rather than the probability of ever getting deeper than the recorded 30-year minimum nadir.) We transform the GEV parameters to reflect the distribution of 30-year, rather than yearly depth values: $\tilde{\sigma} = \sigma\delta^\xi$ and $\tilde{\mu} = \mu + \tilde{\sigma}(1 - \delta^{-\xi})/\xi$ where $\delta = 30$. Figure 10(a) shows $\pi(s, t)$ for values of NAO associated with $x_m(s)$. There are high values of $\pi(s, t)$, especially over western Europe. Figure 10(b) shows $\pi(s, t)$ for NAO = 2, indicating that for a positive NAO phase there is high probability of deeper nadirs over Europe, Iceland and Scandinavia. For NAO = -2, Figure 10(c) attributes high probability of deeper nadirs over Spain, Portugal, west of France and also over the Azores region. Furthermore, Figure 10(d) shows the difference in hPa between the estimated depth limit for MSLP [Figure 10(a)] and $x_m(s)$ for each cell. For most cells, the difference is in the range of 10–50 hPa, while for cells over Iceland the range is 80–110 hPa, indicating the 30-year reanalysis is not long enough to capture nadir depths near the estimated limits.

We use posterior predictive checking Gelman et al. [(2013), Chapter 6] to assess model fit. This compares each observation, $x(s, t)_{\text{obs}}$, to the posterior predictive distribution for replications, $X(s, t)_{\text{rep}}$, of $X(s, t)$ given the

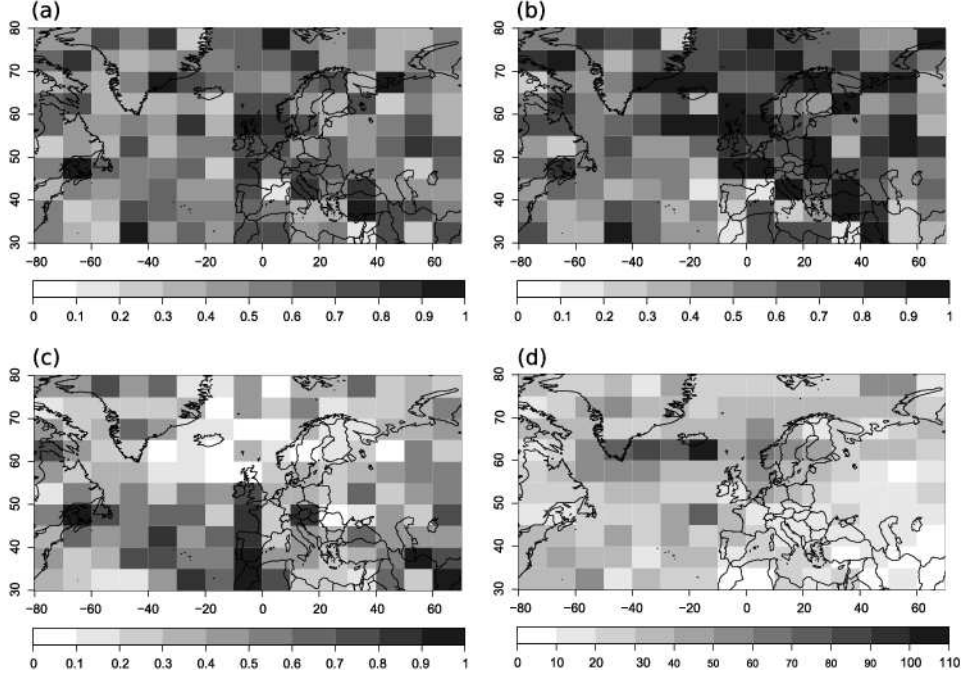


FIG. 10. *Probability of observing a deeper nadir than the recorded 30-year deepest nadir in each cell: (a) Calculated for NAO values associated with the recorded values nadirs, (b) NAO = 2 and (c) NAO = -2. (d) The difference in hPa between the estimated depth limit and the deepest recorded 30-year nadirs in each cell.*

data, D , used to fit the model. If the observations do not behave as if they are sampled from their posterior predictive distributions, then this indicates poor model fit. Samples of $X(s, t)_{\text{rep}}$ were obtained by simulating from GEV distributions with parameters equal to draws from their joint posterior distribution and then the posterior predictive means and 95% posterior predictive intervals were approximated from these samples. We plot the observations of (a) the deepest 30-year nadirs and (b) the deepest yearly nadirs against the corresponding posterior predictive means and intervals in Figure 11(a) and (b), respectively. None of the observations seem extreme with respect to the posterior predictive distributions: the 45-degree line falls well within the prediction intervals.

We also calculate the probability integral transform (PIT), $z(s, t) = \Pr(X(s, t)_{\text{rep}} \leq x(s, t)_{\text{obs}} | D)$, of each observation relative to its posterior predictive distribution. If the model is a good fit, then the $z(s, t)$ should follow a uniform distribution on the interval $(0, 1)$. For each grid cell, s , we plot the probability points $(i - 1)/(n(s) - 1)$ for $i = 1, \dots, n(s)$ against the order statistics of the $z(s, t)$ values for that cell, where $n(s)$ is the number of observations in cell s . Departures from the 45-degree line indicate poor

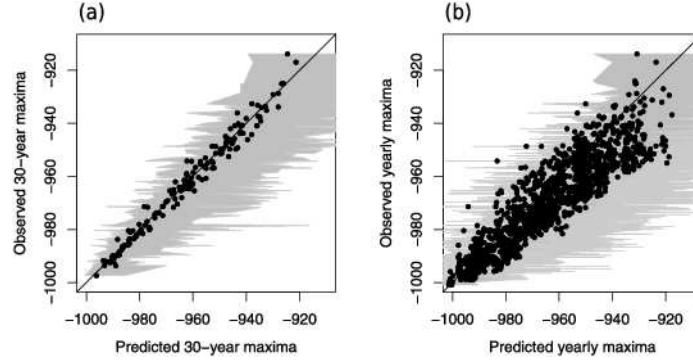


FIG. 11. Recorded versus predicted values of: (a) 30-year deepest nadirs in each cell and (b) yearly deepest nadirs in each cell. The predicted values are the means of the posterior predictive distributions while the grey shaded area represents the associated 95% prediction intervals.

model fit. We indicate the sampling variation that would be expected in these plots when the model is perfect by pointwise 95% confidence intervals, constructed by simulating samples of size $n(s)$ from the uniform distribution on $(0,1)$. Figure 12 shows these plots for Bergen, London and Madrid. No points fall outside the 95% intervals, indicating adequate fit. Note that PIT values are often used in forecast verification; see, for instance, Gneiting, Balabdaoui and Raftery (2007) and references therein. Although histograms are the more conventional way of displaying PIT values, here we only have a few data points for each cell, so we use probability–probability plots.

5. Conclusions. We have implemented a flexible model, adapted from Cooley and Sain (2010), to reanalysis cyclone data in what we believe to be the first study that simultaneously models both the spatial and temporal structure of extreme extra-tropical cyclones. Using (1) spatial random

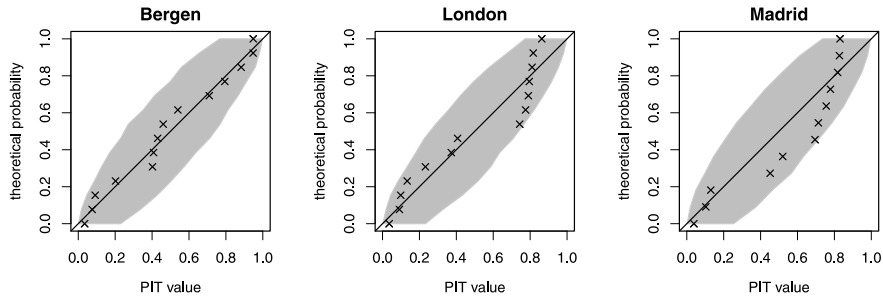


FIG. 12. Probability–probability plots of theoretical $\text{Unif}(0,1)$ probabilities versus probability integral transform (PIT) values $z(s,t)$ for the Bergen, London and Madrid cells. The 95% confidence intervals reflect sampling uncertainty.

effects, (2) latitude as a covariate and (3) a 150 cell spatial regularisation, spatial variation was adequately modelled in the extremal behaviour of the cyclones. The North Atlantic Oscillation was used as a covariate and was found to have a significant effect on extremal cyclone behaviour, especially over Northern Europe and the Iberian peninsula.

Although this is a first step toward studying the spatio-temporal behaviour of extreme cyclones, the analysis relies on assumptions which may oversimplify the problem: (1) the creation of an artificial grid, (2) the choice of threshold in each cell and (3) the subjective choice of spatial proximity. The choice of the grid is a potential weakness which can introduce bias, as both the number of cells and their shape are subjectively chosen. Techniques such as Dirichlet tessellation or Delaunay triangulation [Illian et al. (2008)] may be useful for defining a more optimal “data-driven” grid. The shape of the cells is particularly important if one is interested in modelling data along cyclone tracks rather than individual points as in our application. If interest was in the relative spatial cyclone impact, one could use cell-specific rather than cyclone-specific nadirs, rendering the rectangular cells inappropriate. Hexagonal cells would be more appropriate as illustrated in an application to tropical cyclones in Elsner, Hodges and Jagger (2012). Threshold choice in each cell may also prove to be an issue. Ideally, model fit should be one of the criteria for choosing the threshold. For the application in this paper, three different thresholds were considered: the 85%, 90% and 95% quantile in each cell. Model fit diagnostics (Figures 11 and 12) indicated worse fit for the 85% quantile, and an identical fit for the higher quantiles—which is why we selected the 90% quantile for model implementation. To avoid choosing the threshold altogether, one might instead estimate the threshold from the data. For example, we have explored the possibility of using a mixture model as in Frigessi, Haug and Rue (2002) where the threshold is estimated but which also allows all available data (not just the extremes) to be used for each cell, which in turn allows the use of a finer grid. Last, the proximity structure used to define the covariance matrix of the spatial random effects is also an assumption which can affect the degree of spatial smoothing. The spatially random occurrence of cyclone nadirs was “marginalised” here by dividing the region into grid cells, whereas one should ideally try to model both the spatial occurrence and intensity at the same time, for example, by using spatial marked point process models. Nevertheless, despite these assumptions, the model in this study is flexible enough to be used in other similar studies, for example, ones involving tropical cyclone wind speed maxima or cyclone-related peak precipitation.

APPENDIX

A.1. Point process model for extremes. The point process model for extremes involves a bivariate variable $Y = (X, T)$, with $T \in [0, 1]$ being a

scaled random variable associated with time and $X \in \mathbb{R}$ a random variable associated with intensity. The model is a marked point process, which for $X > u$ (a high threshold) under some linear normalisation and mixing criteria [Smith (1989)] behaves like a nonhomogeneous Poisson process with intensity function

$$(9) \quad \lambda(x, t) = \frac{1}{\sigma} \left[1 + \xi \left(\frac{x - \mu}{\sigma} \right) \right]^{-1/\xi - 1},$$

provided that $1 + (\xi/\sigma)(x - \mu) > 0$. The intensity function $\lambda(x, t)$ is zero for $1 + (\xi/\sigma)(x - \mu) < 0$. The exceedance rate is explicitly modelled in terms of the mean number of exceedances in the time interval $[t_1, t_2]$:

$$\Lambda([t_1, t_2] \times (u, \infty)) = (t_2 - t_1) \left[1 + \xi \left(\frac{u - \mu}{\sigma} \right) \right]^{-1/\xi}.$$

The likelihood given observations $y_i = (x_i, t_i)$ in region $[0, 1] \times (u, \infty)$ is

$$(10) \quad L(\mu, \sigma, \xi; \mathbf{x}, \mathbf{t}) = \exp \left\{ -n_y \int_0^1 \int_u^\infty \lambda(x, t) dx dt \right\} \prod_i \lambda(x_i, t_i)$$

$$(11) \quad = \exp \left\{ -n_y \left[1 + \xi \left(\frac{u - \mu}{\sigma} \right) \right]^{-1/\xi} \right\} \prod_i \lambda(x_i, t_i),$$

where n_y is the number of years of observed data so that parameters μ , σ and ξ correspond to the GEV distribution of yearly maxima. Because the time variable T does not actually appear in (9) and thus in (11), we use the concise notation $X \sim \text{PP}(\mu, \sigma, \xi, u)$ as in Section 3.3. The likelihood contribution from a single event (x_i, t_i) is

$$L(\mu, \sigma, \xi, u) = \exp \left\{ -n_y [t_i - t_{i-1}] \left[1 + \xi \left(\frac{u - \mu}{\sigma} \right) \right]^{-1/\xi} \right\} \lambda(x_i, t_i),$$

for $i = 0, \dots, n$ where n is the number of events. Note that $t_0 = 0$ and that the likelihood contribution, for the time interval between the last event occurrence and $t = 1$, is the probability of no events in the interval, that is,

$$\exp \left\{ -n_y [1 - t_n] \left[1 + \xi \left(\frac{u - \mu}{\sigma} \right) \right]^{-1/\xi} \right\}.$$

The conditional model in (1)–(4) was implemented using the likelihood (11) for each cell. However, because of the temporal covariates, the outermost integral over time in (10) is impossible to calculate analytically unless one knows explicitly how the covariates evolve in time. A remedy is to approx-

imate the integral: divide the time range in small intervals with endpoints $0 = k_1, k_2, \dots, k_J = 1$ and assume the function is constant in each interval. The integral

$$\int_0^1 \left[1 + \xi(s) \left(\frac{u(s) - \mu(s, t)}{\sigma(s, t)} \right) \right]^{-1/\xi(s)} dt$$

is thus approximated by the Riemann sum

$$\frac{1}{J} \sum_{i=1}^J \left[1 + \xi(s) \left(\frac{u(s) - \mu(s, k_i)}{\sigma(s, k_i)} \right) \right]^{-1/\xi(s)},$$

where J is the number of intervals. In practice, J is determined by observations of the covariates for all data (not just the extremes).

A.2. Measures of extremal dependence. The measure of extremal dependence $0 < \chi < 1$ between random variables Z and W is defined as

$$\chi = \lim_{p \rightarrow 1} \Pr(F_Z(Z) > p | F_W(W) > p) = \lim_{p \rightarrow 1} \chi(p),$$

where F_Z and F_W are the respective distribution functions of Z and W . The other extremal dependence measure $-1 \leq \bar{\chi} \leq 1$ is defined as

$$\bar{\chi} = \lim_{p \rightarrow 1} \frac{2 \log \Pr(F_Z(z) > p)}{\log \Pr(F_Z(z) > p, F_W(w) > p)} - 1 = \lim_{p \rightarrow 1} \bar{\chi}(p).$$

If $\chi > 0$ and $\bar{\chi} = 1$, the two variables are asymptotically dependent and χ measures the strength of that dependence. If $\chi = 0$ and $\bar{\chi} < 1$, the two variables are asymptotically independent, in which case $\bar{\chi}$ measures the strength of dependence—within the class of asymptotically independent variables. Roughly, $\bar{\chi}$ measures the “speed” at which $\chi(p)$ approaches zero. Coles, Heffernan and Tawn (1999) advocate the use of both χ and $\bar{\chi}$ as indicators of extremal dependence, providing complementary information on different aspects of that dependence.

A.3. Intrinsic Autoregressive priors. Consider a grid with N cells. If the random effect $\boldsymbol{\phi} = (\phi(1), \dots, \phi(N))'$ is assumed to have an IAR prior, then $\boldsymbol{\phi} \sim N(0, (\tau \mathbf{W})^{-1})$, where \mathbf{W} is the adjacency matrix and the conditional distribution for each $\phi(s)$ given the rest is given by

$$\phi(s) | \boldsymbol{\phi}(-s) \sim N\left(\bar{\phi}(s), \frac{1}{\tau m(s)}\right),$$

where $\boldsymbol{\phi}(-s)$ is $\boldsymbol{\phi}$ excluding $\phi(s)$; $\bar{\phi}(s)$ is the average of $\boldsymbol{\phi}(-s)$ that are adjacent to $\phi(s)$ and $m(s)$ is the number of those adjacencies.

Acknowledgements. We kindly thank Dan Cooley for providing the R code which was adapted for this study and for insightful comments. We also thank Kevin Hodges for providing the track data for NCEP-CFS.

REFERENCES

- BAILEY, T. C. and GATRELL, A. C. (1995). *Interactive Spatial Data Analysis*. Longman, Harlow.
- BANERJEE, S., CARLIN, B. P. and GELFAND, A. E. (2004). *Hierarchical Modelling and Analysis for Spatial Data*. Chapman & Hall, London.
- BONAZZI, A., CUSACK, S., MITAS, C. and JEWSON, S. (2012). The spatial structure of European wind cyclones as characterized by bivariate extreme-value copulas. *Nat. Hazards Earth Syst. Sci.* **12** 1769–1782.
- CASSON, E. and COLES, S. (1999). Spatial regression models for extremes. *Extremes* **1** 449–468.
- COLES, S. (2001). *An Introduction to Statistical Modeling of Extreme Values*. Springer, London. [MR1932132](#)
- COLES, S., HEFFERNAN, J. and TAWN, J. (1999). Dependence measures for extreme value analyses. *Extremes* **2** 339–365.
- COOLEY, D., NYCHKA, D. and NAVEAU, P. (2007). Bayesian spatial modeling of extreme precipitation return levels. *J. Amer. Statist. Assoc.* **102** 824–840. [MR2411647](#)
- COOLEY, D. and SAIN, S. R. (2010). Spatial hierarchical modeling of precipitation extremes from a regional climate model. *J. Agric. Biol. Environ. Stat.* **15** 381–402. [MR2787265](#)
- DAVISON, A. C., PADOAN, S. A. and RIBATET, M. (2012). Statistical modeling of spatial extremes. *Statist. Sci.* **27** 161–186. [MR2963980](#)
- DE HAAN, L. and FERREIRA, A. (2006). *Extreme Value Theory: An Introduction*. Springer, New York. [MR2234156](#)
- DELLA-MARTA, P. M. and PINTO, J. G. (2009). Statistical uncertainty of changes in winter cyclones over the North Atlantic and Europe in an ensemble of transient climate simulations. *Geophysical Research Letters* **36** 1–5.
- DELLA-MARTA, P. M., MATHIS, H., FREI, C., LINIGER, M. A., KLEINN, J. and APPENZELLER, C. (2009). The return period of wind cyclones over Europe. *International Journal of Climatology* **29** 437–459.
- EINMAHL, J. H. J. and MAGNUS, J. R. (2008). Records in athletics through extreme-value theory. *J. Amer. Statist. Assoc.* **103** 1382–1391. [MR2504198](#)
- ELSNER, J. B., HODGES, R. E. and JAGGER, T. H. (2012). Spatial grids for hurricane climate research. *Climate Dynamics* **39** 21–36.
- FRIGESSI, A., HAUG, O. and RUE, H. (2002). A dynamic mixture model for unsupervised tail estimation without threshold selection. *Extremes* **5** 219–235. [MR1995776](#)
- GAETAN, C. and GRIGOLETTO, M. (2007). A hierarchical model for the analysis of spatial rainfall extremes. *J. Agric. Biol. Environ. Stat.* **12** 434–449. [MR2405533](#)
- GELMAN, A., CARLIN, J. B., STERN, H. S., DUNSON, D. B., VEHTARI, A. and RUBIN, D. B. (2013). *Bayesian Data Analysis*. CRC Press, Boca Raton, FL.
- GNEITING, T., BALABDAOUI, F. and RAFTERY, A. E. (2007). Probabilistic forecasts, calibration and sharpness. *J. R. Stat. Soc. Ser. B Stat. Methodol.* **69** 243–268. [MR2325275](#)
- HEATON, M. J., KATZFUSS, M., RAMACHANDAR, S., PEDINGS, K., GILLELAND, E., MANNSHARDT-SHAMSELDIN, E. and SMITH, R. L. (2011). Spatio-temporal models for large-scale indicators of extreme weather. *Environmetrics* **22** 294–303. [MR2843385](#)

- HODGES, K. (1994). A general method for tracking analysis and its application to meteorological data. *Monthly Weather Review* **122** 2573–2585.
- ILLIAN, J., PENTTINEN, A., STOYAN, H. and STOYAN, D. (2008). *Statistical Analysis and Modelling of Spatial Point Patterns*. Wiley, Chichester. [MR2384630](#)
- KATZ, R. W. (2010). Statistics of extremes in climate change. *Climate Change* **100** 71–76.
- LIONELLO, P., BOLDRIN, U. and GIORGI, F. (2008). Future changes in cyclone climatology over Europe as inferred from a regional climate simulation. *Climate Dynamics* **30** 657–671.
- MAILIER, P. J., STEPHENSON, D. B., FERRO, C. A. T. and HODGES, K. I. (2006). The seriality of extratropical cyclones. *Bulletin of the American Meteorological Society* **87** 1317–1318.
- MITCHELL-WALLACE, K. and MITCHELL, A. (2007). Willis’ detailed report for wintercyclone Kyrill. Available at <http://www.willisresearchnetwork.com>.
- NISSEN, K. M., LECKEBUSCH, G. C., PINTO, J. G., RENGGLI, D., ULBRICH, S. and ULBRICH, U. (2010). Cyclones causing wind cyclones in the Mediterranean: Characteristics, trends and links to large-scale patterns. *Natural Hazards and Earth System Science* **10** 1379–1391.
- ODELL, L., KNIPPERTZ, P., PICKERING, S., PARKES, B. and ROBERTS, A. (2013). The Braer cyclone revisited. *Weather* **68** 105–111.
- PINTO, J. G., ZACHARIAS, S., FINK, A. H., LECKENBUSCH, G. C. and ULBRICH, U. (2009). Factors contributing to the development of extreme North Atlantic cyclones and their relationship with the NAO. *Climate Dynamics* **32** 711–737.
- R Development Core Team (2012). *R: A Language and Environment for Statistical Computing*. R Foundation for Statistical Computing, Vienna.
- REICH, B. J. and SHABY, B. A. (2012). A hierarchical max-stable spatial model for extreme precipitation. *Ann. Appl. Stat.* **6** 1430–1451. [MR3058670](#)
- RUE, H. and HELD, L. (2005). *Gaussian Markov Random Fields: Theory and Applications. Monographs on Statistics and Applied Probability* **104**. Chapman & Hall/CRC, Boca Raton, FL. [MR2130347](#)
- SAHA, S. ET AL. (2010). The NCEP climate forecast system reanalyses. *Bulletin of the American Meteorological Society* **91** 1015–1057.
- SANG, H. and GELFAND, A. E. (2009). Hierarchical modeling for extreme values observed over space and time. *Environ. Ecol. Stat.* **16** 407–426. [MR2749848](#)
- SANG, H. and GELFAND, A. E. (2010). Continuous spatial process models for spatial extreme values. *J. Agric. Biol. Environ. Stat.* **15** 49–65. [MR2755384](#)
- SEIERSTAD, I. A., STEPHENSON, D. B. and KVAMSTO, N. G. (2006). How useful are teleconnection patterns for explaining variability in extratropical storminess. *Tellus A* **59** 170–181.
- SIENZ, F., SCHNEIDERREIT, A., BLENDER, R., FRAEDRICH, K. and LUNKEIT, F. (2010). Extreme value statistics for North Atlantic cyclones. *Tellus A* **62** 347–360.
- SMITH, R. L. (1989). Extreme value analysis of environmental time series: An application to trend detection in ground-level ozone. *Statist. Sci.* **4** 367–393. [MR1041763](#)
- SPIEGELHALTER, D. J., BEST, N. G., CARLIN, B. P. and VAN DER LINDE, A. (2002). Bayesian measures of model complexity and fit. *J. R. Stat. Soc. Ser. B Stat. Methodol.* **64** 583–639. [MR1979380](#)
- STEPHENSON, D. B., CASATI, B., FERRO, C. A. T. and WILSON, C. A. (2008). The extreme dependency score: A non-vanishing measure for forecasts of rare events. *Meteorological Applications* **15** 41–50.
- TURKMAN, K. F., TURKMAN, M. A. A. and PEREIRA, J. M. (2010). Asymptotic models and inference for extremes of spatio-temporal data. *Extremes* **13** 375–397. [MR2733939](#)

- ULBRICH, U., FINK, A. H., KLAWA, M. and PINTO, J. G. (2001). Three extreme cyclones over Europe in December 1999. *Weather* **56** 70–80.
- VITOLO, R., STEPHENSON, D. B., COOK, I. M. and MITCHELL-WALLACE, K. (2009). Serial clustering of intense European storms. *Meteorologische Zeitschrift* **18** 411–424.

COLLEGE OF ENGINEERING, MATHEMATICS
AND PHYSICAL SCIENCES
EXETER CLIMATE SYSTEMS
UNIVERSITY OF EXETER
NORTH PARK ROAD
EX4 4QF, EXETER
UNITED KINGDOM
E-MAIL: t.economou@ex.ac.uk
d.b.s.stephenson@ex.ac.uk
c.a.t.ferro@ex.ac.uk